AGU PUBLICATIONS

JGR

Journal of Geophysical Research: Oceans

RESEARCH ARTICLE

10.1002/2016JC011927

Key Points:
- The ocean's interior is reconstructed from observed surface information
- Argo observations are used as test bed
- The isQG method can be applied to the satellite-derived data

Correspondence to:
S. Peng,
speng@scsio.ac.cn

Citation:
Liu, L., S. Peng, and R. X. Huang (2017), Reconstruction of ocean's interior from observed sea surface information, *J. Geophys. Res. Oceans*, *122*, 1042–1056, doi:10.1002/2016JC011927.

Received 1 MAY 2016
Accepted 23 DEC 2016
Accepted article online 29 DEC 2016
Published online 10 FEB 2017

Reconstruction of ocean's interior from observed sea surface information

Lei Liu[1,2], Shiqiu Peng[1,3], and Rui Xin Huang[4]

[1]State Key Laboratory of Tropical Oceanography, South China Sea Institute of Oceanology, Chinese Academy of Sciences, Guangzhou, China, [2]University of Chinese Academy of Sciences, Beijing, China, [3]Laboratory for Regional Oceanography and Numerical Modeling, Qingdao National Laboratory for Marine Science and Technology, Qingdao, China, [4]Woods Hole Oceanographic Institution, Woods Hole, Massachusetts, USA

Abstract Observational surface data are used to reconstruct the ocean's interior through the "interior + surface quasigeostrophic" (isQG) method. The input data include the satellite-derived sea surface height, satellite-derived sea surface temperature, satellite-derived or Argo-based sea surface salinity, and an estimated stratification of the region. The results show that the isQG retrieval of subsurface density anomalies is quite promising compared to Argo profile data. At ~1000 m depth, the directions of retrieved velocity anomalies are comparable to those derived from Argo float trajectories. The reconstruction using surface density input field approximated only by SST (with constant SSS) performs less satisfactorily than that taking into account the contribution of SSS perturbations, suggesting that the observed SSS information is important for the application of the isQG method. Better reconstruction is obtained in the warm season than in the cold season, which is probably due to the stronger stratification in the warm season that confines the influence of the biases in the surface input data (especially SSS) in a shallow layer. The comparison between the performance of isQG with Argo-based SSS input and that with satellite-derived SSS input suggests that the biases in the SSS products could be a major factor that influences the isQG performance. With reduced biases in satellite-derived SSS in the future, the measurement-based isQG method is expected to achieve better reconstruction of ocean interior and thus is promising in practical application.

1. Introduction

The advancement of satellite remote sensing technology during the past decades has revolutionized the way we study the ocean. The ocean surface information, including sea surface height (SSH), temperature (SST), and salinity (SSS), are well sampled with increasing spatial and temporal resolutions and with a global coverage. Because subsurface in situ measurements are still sparse in time and space, projecting the well-sampled satellite-derived sea surface information into the ocean interior serves as an important approach to improve our understanding of the interior ocean dynamics, particularly for the boundary currents which are not adequately measured.

Statistical methods have been employed by several studies to estimate the ocean's interior fields from sea surface data, and reasonable subsurface information is derived [*Carnes et al*., 1990, 1994; *Watts et al*., 2001]. Alternatively, dynamical methods obviating the availability of local historical data have been put forward to provide dynamically consistent interior fields. A number of earlier studies tried to calculate the subsurface structures from surface fields based on sophisticated ocean model dynamics [*Hurlburt*, 1986; *Haines*, 1991; *Cooper and Haines*, 1996]. In the recent decade, a simplified dynamical framework based on the Surface Quasi-Geostrophic (SQG) theory originated in the atmospheric studies [*Held et al*., 1995; *Blumen*, 1978; *Juckes*, 1994; *Hakim et al*., 2002; *Tulloch and Smith*, 2006, 2009] was applied to depict the upper ocean from surface information and yielded promising results [*Lapeyre and Klein*, 2006; *LaCasce and Mahadevan*, 2006; *Isern-Fontanet et al*., 2006, 2008, 2014; *Klein et al*., 2008, 2009; *LaCasce*, 2012; *Ponte and Klein*, 2013; *González-Haro and Isern-Fontanet*, 2014]. The underlying assumption of these methods is that the surface density and interior potential vorticity (PV) are well-correlated, in which case SSH would be in phase with the sea surface

density (SSD) and thus the ocean interior fields can be retrieved through a vertical projection of the surface information. However, there usually exists a phase shift between SSH and SSD (or SST) as noticed by *González-Haro and Isern-Fontanet* [2014] and *Isern-Fontanet et al*. [2014], which may hamper the performance of these SQG-based methods [*Wang et al*., 2013; *Liu et al*., 2014].

The balanced motion in the ocean can be depicted by the Quasi-Geostrophic (QG) framework. Any flow, including the surface flow, is influenced by the total PV field. The interior PV is dominated by the stratification, and the surface PV is related to the surface buoyancy [*Bretherton*, 1966; *Charney*, 1971]. Based on this principle, *Wang et al*. [2013] decoupled SSH and SSD and proposed the "interior + surface QG" (isQG) method for reconstructing subsurface density and velocity from surface density and height. The isQG method first determines the surface contribution from surface density using the SQG approximation. The residual sea surface height (pressure), the difference between the total SSH and the SQG-SSH, is then used to deduce the interior contribution using vertical normal modes. One of the advantages of the isQG method is that the assumption of good correlation between SSH and SSD is not a requirement as in the SQG method. *Wang et al*. [2013] validated this method based on a primitive equation numerical simulation (the Parallel Ocean Program, POP [*Smith et al*., 2000; *McClean et al*., 2002]). A qualitatively good agreement was found between the model output and the isQG reconstruction, especially in energetic regions such as the Gulf Stream Extension. *Liu et al*. [2014] made further validation of the isQG method using two different reanalysis data sets, and investigated the seasonal variation of the isQG performance and its sensitivity to data resolution. *LaCasce and Wang* [2015] simplified the actual stratification using an exponential profile or an exponential with a mixed layer (ML) at the surface, and obtained analytical solutions to the isQG method. The results are generally as good as those of *Wang et al*. [2013], where stratification is directly derived from the model output. *LaCasce and Wang* [2015] also showed that including a surface ML improves density retrievals in the upper ocean. Their results highlight the potential applicability of the isQG method to the real ocean.

Even though the isQG and SQG methods have been proven to be promising, the previous studies show several limitations. (1) The surface density field is required by the methods, but has been proposed to be approximated by surface temperature due to the lack of surface salinity data [*LaCasce and Mahadevan*, 2006; *Isern-Fontanet et al*., 2006, 2008; *González-Haro and Isern-Fontanet*, 2014]. Now the availability of satellite-derived SSS from SMOS (Soil Moisture and Ocean Salinity)/Aquarius (although in coarse resolution and with considerable biases) sheds light on the practical application of the isQG method in reconstructing the ocean interior using real sea surface observations. (2) The validations of isQG method have been done against numerical model outputs only [*Wang et al*., 2013; *Liu et al*., 2014; *LaCasce and Wang*, 2015]. There is a lack of validations against observations.

In this study, we explore the applicability of the isQG method in reconstructing the ocean interior by comparing measurement-based isQG reconstruction against interior Argo observation. The observational data used in isQG method include satellite-derived and Argo-based SSS, satellite SST and SSH. The rest of this paper is organized as follows. Section 2 gives a description of the satellite and in situ data employed in this study, followed by a brief introduction of the isQG method in section 3. The results are presented in section 4 and a summary is given in section 5.

2. Data

2.1. Satellite Data

In this study, we use altimetry absolute dynamic topography (SSH) gridded field provided by AVISO (Archiving, Validation, and Interpretation of Satellite Oceanographic data). The field combines the data from multiple satellite altimeter missions in an objectively mapped grid with 1/4° grid spacing [*Ducet et al*., 2000; *Rio et al*., 2011]. The delayed-mode version of daily SSH field is utilized.

Two Reynolds Optimally Interpolated SST products with a spatial resolution of 1/4° and a temporal resolution of 1 day are provided by the National Oceanic and Atmospheric Administration (NOAA) [*Reynolds et al*., 2007; *Reynolds*, 2009]. One product (AVHRR-only) utilizes in situ and AVHRR (Advanced Very High Resolution Radiometer) data, while the other (AMSR + AVHRR) adds additional AMSR (Advanced Microwave Scanning Radiometer) data. Due to the short record (2002–2011) of AMSR data, we employ the AVHRR-only product here for the year 2012.

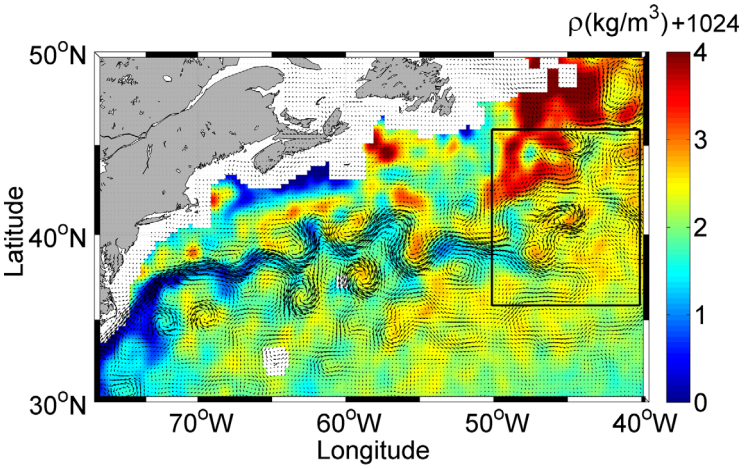

Figure 1. Geographical location of the study region marked by black box (50.125°W–40.125°W, 35.875°N–45.875°N). Overlaid is the geostrophic current field (arrows) derived from altimetry along with the surface density field (color) calculated from SMOS SSS and AVHRR SST, averaged from 31 March to 9 April in 2012.

SMOS satellite was launched in November 2009 and the retrieved SSS data are available from January 2010 to present. In this paper, we use the 10 day composite SMOS Level 3 product (IFREMER V02) with a spatial resolution of 1/4° [*Reul and Ifremer CATDS-CECOS Team*, 2011], which was generated by the Centre Aval de Traitement des Données SMOS (CATDS)/ Expertise Center-Ocean Salinity (CECOS). The accuracy of SMOS SSS data in the western North Atlantic area (77°W–40°W; 30°N–50°N, Figure 1) during 2012 had already been assessed against the in situ measurements by *Reul et al.* [2014], and they found that the bias within the SMOS SSS data over this region exhibits a standard deviation of $\sim$ 0.5 psu.

Note that SMOS product in the western North Atlantic region in 2010 and 2011 was heavily contaminated by the radio frequency interference [*Reul et al.*, 2014], so we only consider the data acquired after 2011; meanwhile, the Argo-based gridded SSS product (see section 2.2) is available only for the period 2002–2012. Therefore, we carry out this study only for the year 2012.

2.2. In Situ Data

Temperature and salinity profiles from Argo floats are provided by the Coriolis Global Data Acquisition Center. For this study, only the profiles with pressure, temperature, and salinity records and a quality control (QC) flag equal to 1 (i.e., considered to be "good") are used.

The In Situ Analysis System (ISAS) was developed to produce gridded fields of temperature and salinity that preserve as much as possible the temporal and spatial sampling capabilities of the Argo global dataset [*Gaillard et al.*, 2009]. Since the first global re-analysis performed in 2009, the system has been extended to accommodate other types of vertical profile (mooring and CTD data). As a comparative ground-truth data set, ISAS-13 gridded (1/2° resolution) monthly fields and climatology of temperature and salinity are employed, which are constructed on 152 levels ranging from 0 to 2000 m depth and entirely based on in situ measurements [*Gaillard*, 2012]. In our study, these 1/2°-resolution products have been interpolated linearly onto a regular 1/4° grid, which is intended to facilitate the comparisons with other fields produced at this spatial scale (i.e., satellite-derived SSH, SST, and SSS). The monthly fields (available for the period 2002–2012) are used to derive stratification profile; the monthly climatology (resulting from an average of ISAS-13 monthly fields over 2004–2012) is used as mean large-scale background field to get the eddy (anomaly) information.

A total of 229 validated Argo profiles with records down to the depth of 1500 m are collected for the year 2012 within the sub-domain (dots in Figure 4a), and vertically interpolated onto the 152 levels of the ISAS-13 products. Meanwhile, 213 profiles with salinity records in the upper 10 m of the ocean are collected for the assessment of SMOS SSS (following section 2.3). In this study, the practical salinity scale (PSS-78) is adopted, and salinity is defined as a conductivity ratio, which is unitless.

Besides the temperature and salinity observations, Argo floats also provide velocity information. We use the velocity product derived from trajectories of Argo floats at their parking level, YoMaHa'07. This product was estimated from the distance divided by the time between the last Argo position fix and the first position fix of two consecutive cycles, with an approximate 10 day sampling period [*Lebedev et al.*, 2007].

Table 1. Statistics of ISAS SSS (Monthly, 1/2° × 1/2°) and SMOS SSS (10 Day, 1/4° × 1/4°) With Respect to Argo SSS During 2012[a]

	Mean(△SSS)	Std(△SSS)	RMSE	Correlation Coefficient	N
SMOS	0.28	0.71	0.74	0.82	213
ISAS	0.14	0.38	0.42	0.95	213

[a]$\triangle SSS = SSS_{SMOS/ISAS} - SSS_{Argo}$.

The monthly gridded dataset (1° × 1°) for velocity based on Argo observations, AGVA (Absolute Geostrophic Velocities from Argo), was distributed by the University of Washington [*Gray and Riser*, 2014]. AGVA currently provides data spanning December 2004 to November 2010 on 29 pressure surfaces from 5 dbar to 2000 dbar. In this study, we employ AGVA to derive the velocity climatology serving as mean large-scale background.

2.3. Assessment of SMOS SSS

The accuracy of SMOS SSS in the study region is assessed by comparing the satellite products with salinity measurements from Argo floats. Satellites measure T/S at the first centimeter or skin layer of the sea surface, while the typical top level observed by Argo floats is about 5 m depth. In this paper, we use the closest Argo T/S to the sea surface in the upper 10 m of the ocean to represent the surface value, without any interpolation to the surface (the same way employed by *Boutin et al*. [2013]). The SMOS SSS maps are linearly interpolated to the locations of Argo measurements acquired within the corresponding 10 day time window. For comparison, we also interpolate the ISAS monthly SSS fields the same way, but using 1 month time window. Table 1 lists the statistics of SMOS/ISAS SSS collocated with Argo SSS acquired in 2012 (213 collocations). SMOS SSS data are saltier than Argo SSS with a mean positive bias of 0.28. The correlation between Argo SSS and SMOS SSS is strong with a correlation coefficient of 0.82 (significant at 0.05 confidence level). The root mean square error (RMSE) for SMOS SSS is quite large (0.74), which is mainly caused by the degraded accuracy of this product during the coldest months of the year [*Reul et al*., 2014]. Although the collocations in time are much less precise for monthly ISAS SSS, the statistics are better than those of SMOS. In this study, each of these two different SSS products, combined with satellite-derived SST and SSH, is used as input of isQG to check the influence of SSS biases on the isQG performance.

2.4. Data Preprocessing

Figure 2 illustrates how the data listed above in section 2.1 and 2.2 (gray-shaded boxes in Figure 2) are processed in this study. We first handle the data to derive sea surface height eddy (anomaly) field (SSHA) and sea surface density eddy field (SSDA) required for the isQG reconstruction. To be consistent with the 10 day composite of SMOS SSS data, satellite-derived daily SST and SSH are processed to generate 36 groups of 10 day-mean fields in the year 2012. Meanwhile, SSH climatology is constructed from daily SSH over the period of 2004–2012 (coincident with ISAS climatology). Currently, the resolution of gridded SSH using two altimeters is confined to scales larger than 150 km, and it is not possible for the gridded SSH to observe wavelengths smaller than 120 km even with a constellation of nadir altimeters [*Ducet et al*., 2000; *Chelton and Schlax*, 2003; *Chavanne and Klein*, 2010; *Dibarboure et al*., 2011; *Gaultier et al*., 2016]. Figure 3 shows the zonal wavenumber spectra of the 10 day-mean SSH, SST, and SMOS SSS, which are calculated using 256 samples along 39.625°N (72°W–8°W) for the period of 31 March to 9 April. The spectral slopes between 150 and 400 km wavelengths are then calculated via a least squares fit of a power law (dashed lines). In the mesoscale band, although the spatial resolution of gridded SSH is not high, SSH wavenumber spectral slope with a value of −2.9 is closer to the $k^{-11/3}$ law than to the k^{-5} law, indicating the validity of the SQG theory [*Le Traon et al*., 2008]. In SQG theory, assuming SST dominates SSD, SST (SSD) should present a spectral slope of $k^{-5/3}$ [*Blumen*, 1978], and the SST spectral slope (−2) computed here is close to the −5/3 value. For SSS, the slope is flat (−1.1) and evident power can be found at scales smaller than 120 km, which could be caused by noises in the SMOS product. The 10 day-mean SST is combined with SMOS SSS to produce SSD (denoted as SMOS-SSD). Figure 1 shows the 10 day composite of satellite SSD field from 31 March to 9 April in 2012, superimposed with the concurrent distribution of geostrophic flows estimated from altimetry. As seen in Figure 1, there is a good negative correlation between the SSH and density fields, i.e., negative sea level anomalies with cyclonic flows correspond to the denser seawater. This agrees with the results of recent studies [*Isern-Fontanet et al*., 2008, 2014], which show that the phase shift between SST and SSH is minimum for deep ML (winter time). As to another experiment using ISAS monthly SSS instead of SMOS 10 day composite SSS, the monthly SSS is projected into 10 day-mean fields using linear interpolation to generate the corresponding SSD (denoted as ISAS-SSD). In order to get mesoscale eddy fields (SSHA and SSDA), the

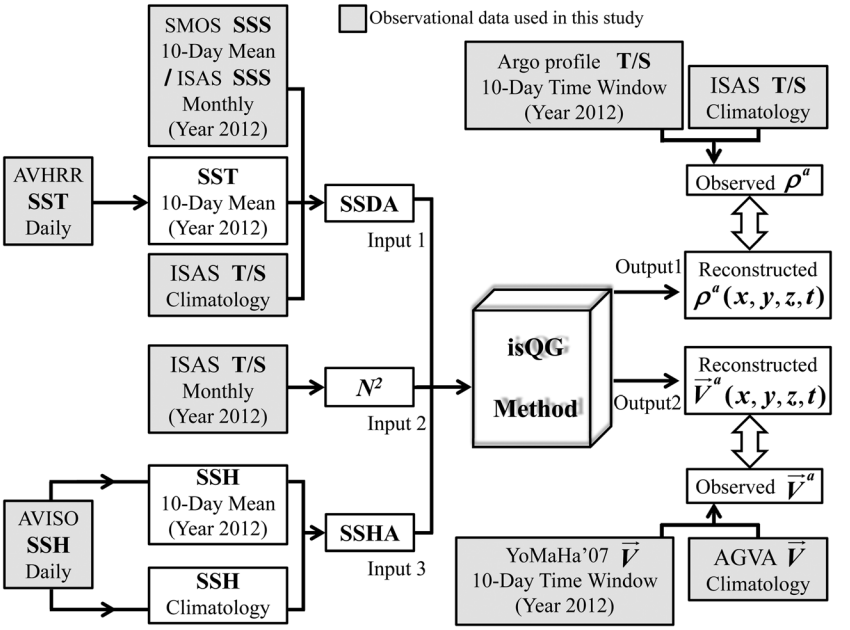

Figure 2. A flowchart for the isQG performance evaluation. Gray-shaded boxes denote the observational data used in this study.

monthly climatology is linearly interpolated into 10 day-mean fields and removed (SSD climatology is derived from ISAS T/S climatology).

In addition to SSDA and SSHA, the vertical stratification profile N^2 is also required for the input of the isQG reconstruction. We first linearly interpolate the ISAS monthly T/S fields into 10 day-mean dataset and calculate potential density at different levels. Then these density fields are employed to calculate the local $N^2(x, y, z, t)$ for corresponding 10 day composite datasets (SSDA, SSHA) using the mean pressure between two vertical grids as the reference pressure:

$$N^2(x,y,z,t) = -\frac{g}{\bar{\rho}(x,y,t)}\frac{\partial \rho(x,y,z,t)}{\partial z}, \quad (1)$$

where $\bar{\rho}$ is the vertical mean of potential density, and g the gravity constant. Modification is made to the stratification profiles near the surface where $N^2(x, y, z, t)$ generally approaches zero using a linear interpolation [*Wang et al.*, 2013; *Liu et al.*, 2014].

Now the isQG can be numerically solved given the three input variables (SSHA, SSDA, and N^2). To evaluate the isQG-retrieved density eddy (anomaly) fields in the interior ocean, observed density anomalies calculated from Argo T/S profiles and ISAS T/S climatology are used, with the density profiles from Argo smoothed by a 40-m running mean to remove the influences of internal waves. For the evaluation of retrieved velocity anomaly fields,

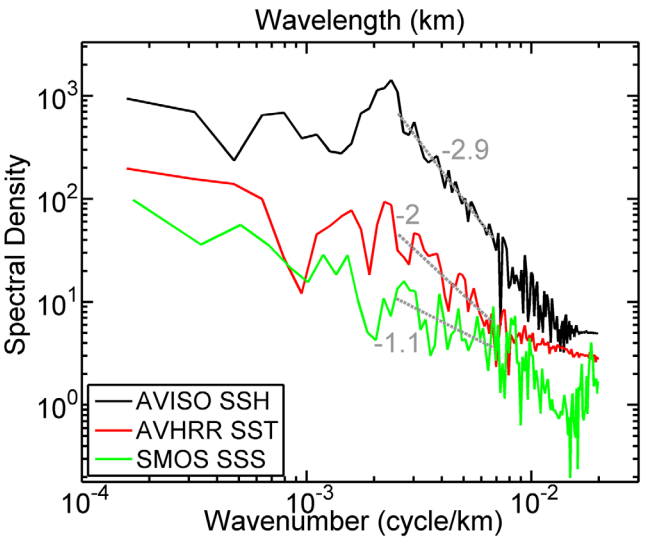

Figure 3. Wavenumber spectra of the 10 day-mean SSH (black line) and SST (red line), as well as SMOS SSS (green line) for the period of 31 March to 9 April in 2012, calculated respectively from 256 samples along 39.625°N (72°W–8°W). Units on the vertical axis are $(cm)^2$/cycle/km for SSH, $(°C)^2$/cycle/km for SST, and 1/cycle/km for SSS. The dashed lines are linear fits in the wavelength range of 150–400 km. The values of the spectral slope are noted in the plot.

YoMaHa'07 trajectories-based velocities and AGVA velocity climatology are employed. The AGVA velocity climatology was constructed over a shorter period (2004–2010) compared with ISAS climatology (2004–2012). However, that will not cause problems due to the weak background (velocity) signals relative to the mesoscale signals in the open ocean. To be temporally consistent with the 10 day composite input (SSHA, SSDA), we group the Argo profiles and YoMaHa'07 velocities by a 10 day time window. The density (velocity) climatology from ISAS (AGVA) is linearly interpolated first into 10 day mean fields and then into the position of each Argo float in the corresponding time slot, and then is removed from Argo-derived density (velocity) to produce the observed density (velocity) anomalies.

3. The isQG Method and Experiment Setup

The isQG method [*Wang et al*., 2013] is employed in this study to reconstruct subsurface density and velocity from sea surface density and height. This method is based on the Quasi-Geostrophic framework and the principle that the total PV of the balanced motion in ocean can be decoupled into a surface component associated with the surface buoyancy and an interior component dominated by stratification. The isQG method first determines the surface contribution from surface density using the SQG approximation, and the residual sea surface height (pressure) is then used to deduce the interior contribution using vertical normal modes. A brief description of isQG method is given in Appendix A and a more detailed one can be found in previous studies [e.g., *Wang et al*., 2013; *Liu et al*., 2014].

Our study focuses on the sub-domain of the Gulf Stream region with a size of $10^\circ \times 10^\circ$ (black box in Figure 1) that is far away from continental boundaries and full of energetic eddies. The ocean interior reconstructions are done every 10 days for the whole year of 2012 using 10 day-mean surface data sets (i.e., SSH, SST, and SSS). Biases or uncertainties could exist in all the three input variables of the isQG method, i.e., the satellite-derived SSH maps, the satellite-derived SSD (including SST and SSS) gridded fields, and the monthly $N^2(x, y, z, t)$. While it is difficult to assess directly the impacts of the biases in SSH fields on the reconstruction in this study, the impacts of biases in the satellite-derived SSD and the monthly $N^2(x, y, z, t)$ can be roughly assessed by utilizing Argo-derived SSD and $N^2(x, y, z, t)$ as inputs of the isQG method and validating the reconstruction against the original Argo profiles, with the assumption that the Argo-derived SSD and $N^2(x, y, z, t)$ are unbiased. For this purpose, employing SSD derived from instantaneous Argo observations as input, we first carry out two types of reconstructions (denoted as isQG-Argo and isQG-Argo-N^2) with the N^2 input respectively derived from monthly mean and real-time (Argo) observations. Subsequently, we carry out reconstructions using two kinds of satellite-derived SSD (i.e., SMOS-SSD and ISAS-SSD). To further investigate the benefit of observed SSS information (SMOS and ISAS) to the isQG performance, we carry out the fifth reconstruction (denoted as isQG-AVHRRonly) utilizing the SSD derived from AVHRR SST and constant SSS (estimated from ISAS monthly data), which excludes the influences of observed salinity information, the same way as *Isern-Fontanet et al*. [2006] did.

4. Validation of Retrieved Density and Velocity Fields

4.1. Density Anomalies

Employing density anomalies derived from 229 Argo profiles in the year 2012 as test beds, we evaluate the retrieved density anomaly fields which are interpolated to the location of each profile measurement (dots in Figure 4a) using a linear spatial interpolation. Specifically, to assess the seasonal variability of the reconstruction, we divide the year 2012 into two seasons: the cold season (1 January–9 May, 6 November–25 December) and the warm season (10 May–5 November), according to the seasonal variations of mixed layer depth (MLD), stratification, and the spatial correlation between SSHA and SSDA over the study region: deeper ML with weaker stratification and stronger anti-correlation (less phase shift) between SSHA and SSDA in the boreal winter (Figure 4b).

Half of the 36 sets of 10 day composite fields in 2012 are grouped into the cold season with 107 of 229 Argo profiles. The similarities between isQG-Argo and observations are quantified in Figure 5a, which shows the correlation coefficients (black line) between the retrieved density anomalies and 107 profiles of Argo measurements as a function of depth (gray denotes correlations not significant at 0.05 confidence level). The correlation with a value of 1.0 can be found at 0 m as expected, since the isQG solution at surface is identical to the SSDA input, i.e., the Argo density anomaly at the surface. In the ML, the correlations

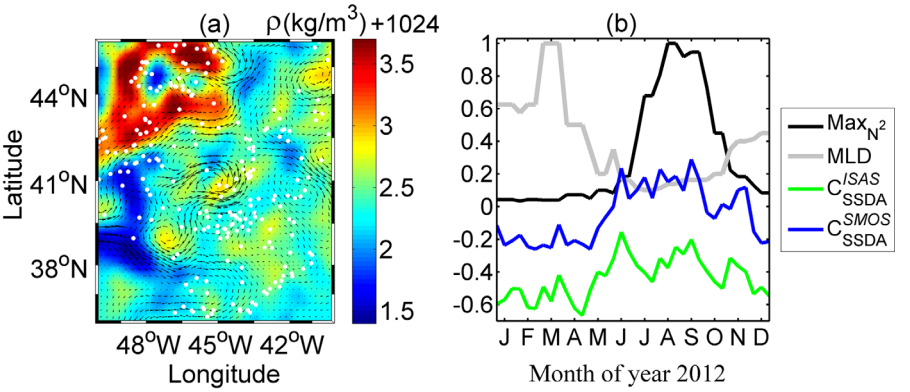

Figure 4. (a) Surface density field (color) and geostrophic currents (arrows), averaged from 31 March to 9 April in 2012, for the study region, superimposed with locations of 229 Argo profiles (white dots) in 2012. (b) Temporal variations of mixed layer depth (gray line), maximum value of stratification (black line), correlation coefficients between SSDA derived from SMOS SSS and SSHA (blue line), and between SSDA derived from ISAS SSS and SSHA (green line) from January 2012 to December 2012 for the study region. The mixed layer depth and maximum values of stratification are scaled by their maximum values, respectively, i.e., 200 m and 65.02 $\times$ 10^{-5} s^{-1}.

decrease with depth and maintain small values ($<$0.5) between 90 and 210 m depths. Strong correlations ($>$0.5) can be found between 220 and 1380 m depths with a maximum of 0.68 at 450 m depth. Performance of the isQG-Argo degrades below 1380 m and the correlations decrease rapidly to 0.1 around 1500 m depth. Because the correlations do not reflect the amplitude difference, we also compare the vertical profile of the root-mean-square (RMS) of density anomalies obtained from isQG-Argo (black line) with that from in situ measurement (red line) in Figure 5b. Although discrepancies exist, Figure 5b illustrates that the isQG solution can reasonably reflect the amplitudes of the observed density anomalies.

Local stratification $N^2(x, y, z, t)$ diagnosed from gridded monthly fields may smooth out small-scale structures. For some case studies (not shown) when the real-time vertical profiles of stratification are much different from those derived from monthly mean, incorporating N^2 information from in situ observations can improve the reconstruction, especially in the ML where small-scale signals are prominent. Therefore, we replace the ISAS monthly mean N^2 used in isQG-Argo with instantaneous N^2 derived from Argo floats to assess the effect of employing more realistic stratification on the isQG performance. Statistical results in Figure 5 show that, compared with isQG-Argo using monthly mean N^2 (black lines), the usage of N^2 derived from Argo floats leads to a slightly refined reconstruction (isQG-Argo-N^2, green lines). In the upper 210 m, stronger correlations are obtained using Argo-derived N^2. Between 220 and 480 m depths, although

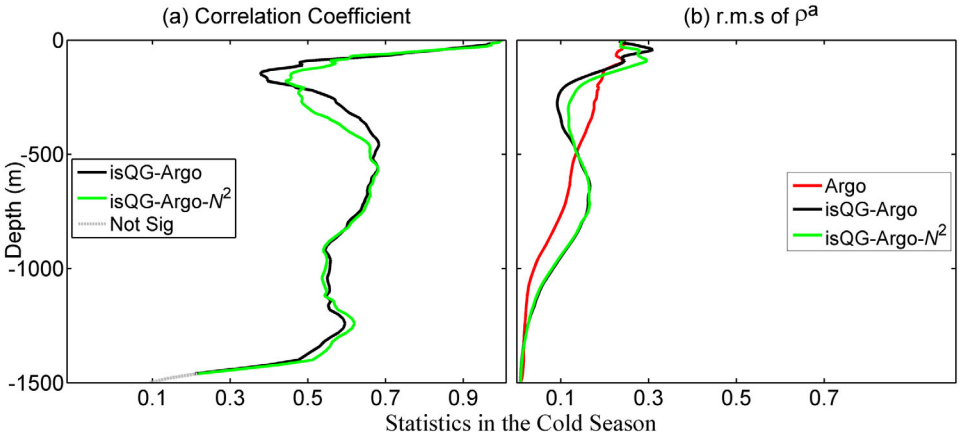

Figure 5. (a) Correlation coefficients between the retrieved density anomalies and 107 profiles of Argo measurements as a function of depth in the cold season. Gray denotes correlations not significant at 0.05 confidence level. (b) The RMS of the density anomalies derived from isQG solutions and from Argo observations (red line) in the cold season. Black lines stand for retrieval using SST/SSS from Argo profiles, and N^2 from monthly mean; green lines denote retrieval employing SST, SSS, and N^2 all from Argo profiles.

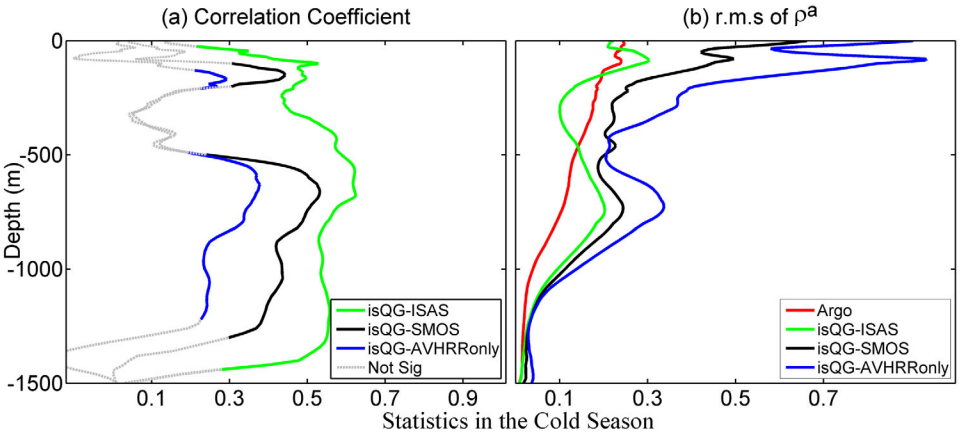

Figure 6. (a) Correlation coefficients between the retrieved density anomalies and 107 profiles of Argo measurements as a function of depth in the cold season. Gray denotes correlations not significant at 0.05 confidence level. (b) The RMS of the density anomalies derived from isQG solutions and from Argo observations (red line) in the cold season. All the retrievals are based on monthly mean N^2. Green lines stand for retrieval using AVHRR SST and ISAS SSS; black lines denote retrieval employing AVHRR SST and SMOS SSS; and blue lines denote retrieval utilizing AVHRR SST along with a constant salinity distribution.

correlations are slightly weaker for isQG-Argo-N^2, the RMS profile for this retrieval is closer to the Argo observations (red line) than that for isQG-Argo.

With the influences of both SSDA biases and stratification biases excluded, differences between isQG-Argo-N^2 and Argo observations could arise from the 10 day-mean SSH. For some locations (not shown) near the periphery of eddies, isQG-Argo-N^2 does not perform satisfactorily. Spatial uncertainties in the gridded SSH (due to the optimal interpolation for generating the two-dimensional maps), especially near the edges of eddies, can cause a spatially shifted reconstruction. Differences could also be caused by the deficiency of only two dynamical modes for the interior solution, particularly in the near-surface region.

Because the monthly mean can be more readily accessed and provide reasonable estimates of the stratification within a region for a particular month, we employ the monthly mean stratification hereafter in other retrieval experiments for practical purpose.

Using SMOS-SSDA (or ISAS-SSDA) as input, retrieval denoted by isQG-SMOS (or isQG-ISAS) is carried out and the statistical results are presented in Figure 6. It is found that isQG-ISAS achieves a better performance than isQG-SMOS in terms of seasonal statistics with higher correlation and less root-mean-square deviation. For isQG-ISAS (green line), the correlations, which are weak near the sea surface, increase with depth in the upper layers and reach 0.5 around 100 m depth. Strong correlations ($>$0.5) are obtained between 340 and 1380 m depths with a maximum of 0.63 around 700 m depth. Quality of the reconstruction deteriorates below 1380 m and the correlations decrease to 0.03 around 1500 m depth. The correlations for isQG-SMOS (black line) are relatively weak as a whole, with values exceeding 0.5 between 600 and 750 m depths and a maximum of 0.53 around 650 m. For isQG solution, the RMS of density anomaly at the surface is exactly the one from gridded SSDA input of isQG, thus the difference between isQG solution (green and black lines) and Argo observations (red line) at the surface indicates biases in the gridded SSDA input. The RMS profile for isQG-ISAS (green line) is closer to the Argo observations than isQG-SMOS (black line). Large discrepancies between the Argo observations and the solution based on SMOS SSS are found at the surface, which could be attributed to larger biases in the SMOS product with a notable RMSE of 0.74 as shown in Table 1.

As to the retrieval from isQG-AVHRRonly, SSDA input exhibits larger bias at the surface due to the usage of constant salinity compared with that for isQG-ISAS or isQG-SMOS (blue line in Figure 6b), leading to the weakest correlations (blue line in Figure 6a) in the interior ocean. These results suggest that including the observed SSS information is quite important and necessary to the application of the isQG method in the real ocean, although considerable biases still exist in the current SSS products (especially SMOS SSS).

Compared with statistics for isQG-Argo (Figure 5), biases in the SSDA input of isQG-ISAS, isQG-SMOS and isQG-AVHRRonly lead to degraded reconstructions (weaker correlations and larger RMS deviation, Figure 6). During the boreal cold season, deep ML and weak stratification may enhance the penetration of SQG

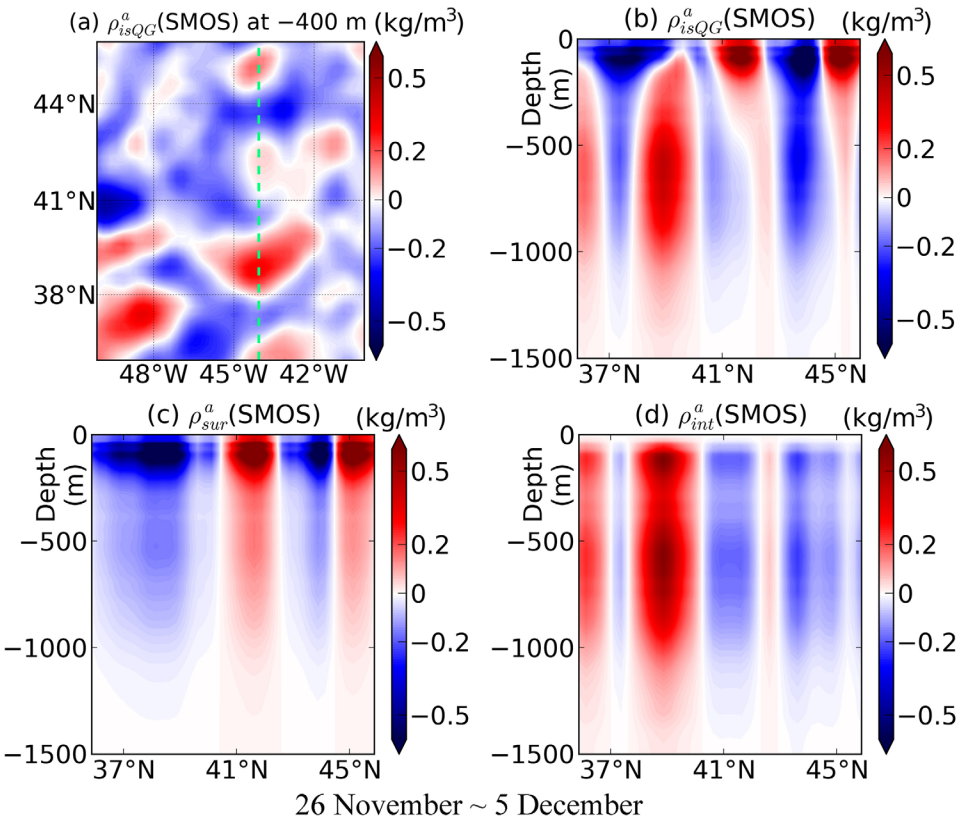

Figure 7. (a) Retrieved density anomalies at 400 m depth, with the SSDA input derived from AVHRR SST and SMOS SSS for the period of 26 November to 5 December in 2012. Vertical sections of the retrieved density anomalies at 44.1°W from (b) isQG combined solution, (c) SQG solution, and (d) interior solution. Dashed line in Figure 7a marks the location of the vertical section.

solution into the deeper layers. As shown in Figure 7, the SQG solution is evident down to ~ 900 m depth (Figure 7c). Therefore, the SSDA biases that incorporated into the SQG solution may propagate into deeper layers, leading to large differences between reconstructions and subsurface observations. In addition, for isQG-SMOS, large errors in SMOS SSS which are transformed to SSD might cause very low correlations between SMOS-SSDA and SSHA (comparing blue and green lines in Figure 4b). Low correlation between SSDA and SSHA is a sign that the SQG portion of the isQG reconstruction may be not that good.

For the warm season, the performances of the isQG method with different combinations of input data are similar to those for the cold season, with stronger correlations down to 1400 m depth (Figure 8). It is interesting to note that, in the warm season, the retrieval isQG-SMOS is nearly identical to, or even slightly better (between 700 and 1300 m depth) than that from isQG-ISAS, with strong correlations (>0.5) between 70 and 1420 m depth and a maximum of larger than 0.74 around 550 m (Figure 8a). The good performance of isQG-SMOS in the warm season could be primarily attributed to the improvement of SMOS SSS accuracy in summer [*Reul et al*., 2014], as indicated by nearly the same RMS value at 0 m for both isQG-SMOS and isQG-ISAS (Figure 8b) which suggests that the accuracy of SMOS-SSDA (or SMOS SSS) is comparable to that of ISAS-SSDA (or ISAS SSS). Moreover, notably for isQG-AVHRRonly, SSDA biases are quite large (blue lines at 0 m), but the retrieval below 400 m depth is closer to that of isQG-SMOS or isQG-ISAS than in the cold season. According to the isQG dynamics, this method is presumably more effective during winter when the ML is deeper with weaker stratification, while it is slightly degraded during summer with shallower ML and stronger stratification [*Wang et al*., 2013; *Liu et al*., 2014]. The reverse results presented here, i.e., better performance of the isQG method in the warm season, are probably caused by that (1) SSDA biases incorporated into the SQG solution are constrained within shallow layers by strong stratification and shallow ML in the warm season, as demonstrated in Figure 9 which shows that the influencing depth of the SQG solution is much shallower (Figure 9c) than that in the cold season case (Figure 7c); (2) the SSHA field (employed by isQG-SMOS, isQG-ISAS, and isQG-AVHRRonly) in the warm season mostly reflects interior solution that

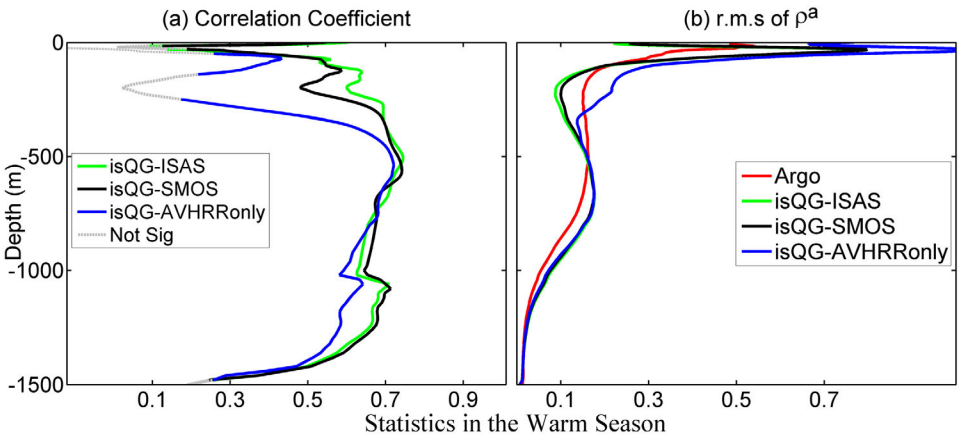

Figure 8. The same as Figure 6, but for retrievals in the warm season when 122 profiles of Argo measurements are employed.

dominates below the ML, as indicated by the large phase shift between SSDA and SSHA in summer [*Wang et al.*, 2013; *Liu et al.*, 2014].

For both of the cold and warm seasons, the retrievals have obvious discrepancies in the near-surface region. This could partly be attributed to the linear modification for N^2 profiles in the ML applied in this paper. It is expected that including a more realistic ML component as done in *LaCasce and Wang* [2015] may increase the accuracy of the reconstruction, which will be tested in a separate study.

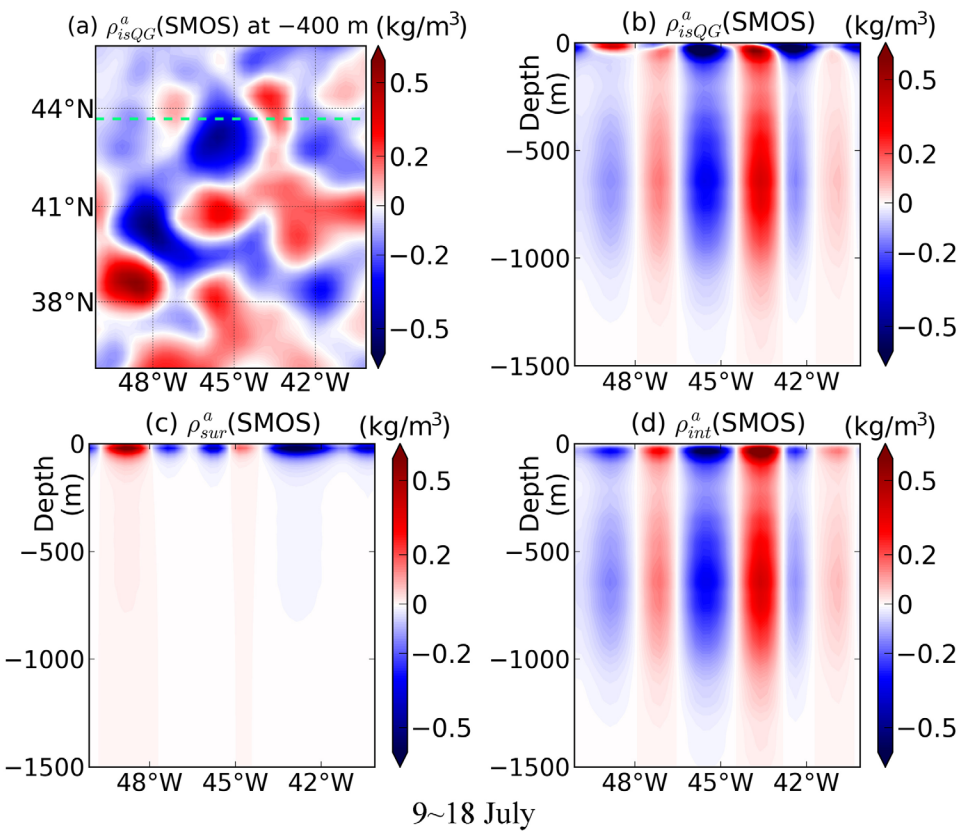

Figure 9. The same as Figure 7, but for the period of 9 to 18 July in 2012. Dashed line in Figure 9a marks the location of the vertical section at 43.7°N.

Table 2. Statistics of the Retrieved Velocity Anomalies at Argo Parking Depth With Respect to 130 Velocity Anomaly Observations Derived From Trajectories of Argo Floats During 2012[a]

	Direction			Strength			
	Mean |△Dir|	Std |△Dir|	RMSE	Mean △Str	Std △Str	RMSE	Mean RD
isQG-ISAS	33.07	23.09	40.28	−0.06	0.05	0.08	62.7%
isQG-SMOS	38.21	30.91	49.07	−0.06	0.05	0.07	60.9%
isQG-AVHRRonly	39.84	33.52	51.98	−0.06	0.05	0.08	62.1%

[a]$\triangle Dir = Direction_{isQG} - Direction_{Traj}$ (unit: degree); $\triangle Str = Strength_{isQG} - Strength_{Traj}$ (unit: m/s).

4.2. Velocity Anomalies

Due to the sparse observations for velocity in the study region, we statistically evaluate the performance of the velocity retrieval against all the available 130 Argo trajectory data at Argo parking depth (∼1000 m) during the year 2012, regardless of the seasonal variation. Table 2 demonstrates that the directions of observed currents are reasonably captured by the isQG method, with the mean of absolute direction differences ($|\Delta Dir|$, not larger than 180°) between the retrieved and observed currents less than 40° and the isQG-ISAS slightly outperforming the isQG-SMOS (consistent with discussions in section 4.1). However, for the current strength, the performance of the isQG method is less satisfactory. The retrieved currents are generally weaker than the observed one, with mean strength biases of −0.06 m/s and mean relative deviations (RD) exceeding 60%.

At the Argo parking depths (∼ 1000–1500 m), the isQG solution is mostly determined by the interior solution component. The deficiency of only two dynamical modes for the interior solution can degrade the performance in the deep layers, especially for the current strength. Meanwhile, the biases with unknown structures in the gridded SSH fields also affect the velocity retrieval in the deep ocean. On the other hand, large uncertainties may exist in the velocity observations derived from Argo trajectories, leading to large biases in the evaluation of velocity retrieval.

5. Summary and Discussion

In this paper, we apply the isQG method to retrieve the ocean subsurface density/velocity anomaly (eddy) fields in the spatial range between 150 and 400 km using observations. The observational data include the sea surface information from satellite (AVISO SSH, AVHRR SST, and SMOS SSS), surface temperature/salinity monthly and climatology fields constructed from in situ measurements (ISAS-13), and an estimate of vertical stratification diagnosed from monthly fields (ISAS-13). To investigate the benefit of observed SSS information (SMOS and ISAS) to the isQG performance, as well as the impacts of the SSS or stratification biases on the isQG performance, we carry out a set of experiments of retrievals using different input SSD or stratification derived from Argo T/S profiles or AVHRR SST + SMOS SSS/ISAS SSS/constant salinity. Retrieved density and velocity anomalies are validated against Argo profile and trajectory data respectively in a region away from continental boundaries in the western Atlantic. The results are summarized as follows:

1. The retrieval experiment using SSDA input derived from Argo profiles and N^2 input derived from monthly mean, which excludes the influences of SSDA biases, demonstrates that the isQG method is effective in retrieving the subsurface density from sea surface information. Below the base of ML and down to a depth of about 1400 m, the isQG reconstruction satisfactorily captures the structure of observed density anomalies with correlation coefficients exceeding 0.5. Replacing monthly mean N^2 with N^2 derived from real-time observations (Argo profiles) only slightly improves the statistical results, indicating the usefulness of the monthly mean N^2 in the practical application of the isQG method in the real ocean.
2. Retrievals using different SSDA input respectively derived from AVHRR SST + SMOS SSS and AVHRR SST + ISAS SSS are better than the retrieval using SSDA derived from AVHRR SST + constant SSS. This indicates that including the observed SSS information is quite necessary and important for the application of the isQG method.
3. Seasonal variability is obvious in the performance of the isQG method. Generally, the isQG performs better in the warm season than in the cold season, probably due to strong stratification in the warm season that suppresses the vertical propagation of SQG solution and thus confines the influence of the biases

from surface data in very shallow layers. In particular, the retrieval from isQG-SMOS is much less satisfactory than that from isQG-ISAS due to large biases in SMOS in the cold season; however, they are comparable to each other in the warm season with improved accuracy of SMOS SSS in summer [*Reul et al.*, 2014], or even isQG-SMOS outperforms isQG-ISAS at some locations with good quality of SMOS SSS, highlighting the bright prospects of the isQG method with increasingly improved accuracy of the satellite-derived SSS in the future.

4. At the Argo parking depth ($\sim$ 1000 m), the retrieved velocity anomalies are comparable to the velocities from Argo float trajectories in terms of current direction, with mean direction difference less than 40°.

The reconstruction results based on the isQG method with its input all from observational data are encouraging and highlight the practical applications of isQG method in the real ocean for the first time. With the advance of satellite remote-sensing techniques in the coming future, increasingly improving accuracy with higher spatial resolution for the satellite-derived sea surface data is expected (especially for the SSS data from SMOS or Aquarius), which makes this method more promising. Moreover, given that only the barotropic and first baroclinic modes are considered in the interior portion of the isQG method, a prospective way to further improve the performance of the isQG method is to add more baroclinic modes in the interior solution to fully represent the ocean interior.

In addition to the SSDA biases, the biases with unknown structures in the gridded SSH fields generated from one-dimensional SSH measurements along the satellite track can also degrade the isQG performance, especially in the deep layers, which could cause the much weaker strength of the retrieved velocities at $\sim$ 1000 m depth than that of trajectory data. The satellite mission called SWOT (Surface Water and Ocean Topography) to be launched in 2020, which aims at measuring high-resolution SSH in two dimensions along a wide swath [*Fu and Ubelmann*, 2014; *Qiu et al.*, 2016], will help to reduce the SSH biases and thus improve the isQG performance. The above-mentioned issues will be investigated in our future work.

Appendix A: A Brief Introduction of the isQG Method

Assuming that the flow is in QG equilibrium, the stream function is related to PV by:

$$\left(\frac{\partial^2}{\partial x^2}+\frac{\partial^2}{\partial y^2}+\frac{\partial}{\partial z}\frac{f_0^2}{N^2}\frac{\partial}{\partial z}\right)\Psi=q(x,y,z,t) \tag{A1}$$

[*Pedlosky*, 1987] where f_0 is the Coriolis parameter, $N(z)$ the Brunt-Väisälä frequency, $\Psi=p/(f_0\rho_0)$ the geostrophic stream function, and q the anomaly from the large-scale background PV. In the definition of stream function, p and ρ_0 denote the pressure anomaly and the reference density, respectively. Due to the linearity of the QG PV equation, Ψ can be written as the superposition of a homogeneous solution called surface (SQG) solution (Ψ^{sur}) and a particular solution named interior solution (Ψ^{int}) [*Hoskins*, 1975; *Lapeyre and Klein*, 2006; *Ferrari and Wunsch*, 2010; *Wang et al.*, 2013]. To obtain the stream function field, appropriate boundary conditions are required:

$$\left.\frac{\partial\Psi^{sur}}{\partial z}\right|_{z=0}=\frac{b^s}{f_0},\left.\frac{\partial\Psi^{sur}}{\partial z}\right|_{z=-H}=\frac{b}{f_0}=0, \tag{A2a}$$

$$\left.\frac{\partial\Psi^{\mathrm{int}}}{\partial z}\right|_{z=0,\,-H}=0. \tag{A2b}$$

Where $b=-g\rho/\rho_0$ is the buoyancy anomaly with ρ being the density anomaly; b^s is the buoyancy anomaly at surface. For the bottom boundary ($z=-H$) condition, density anomaly is neglected. The lateral boundary conditions are simplified to be doubly periodic, which is reasonable for a sub-domain in the open ocean.

In the Fourier space, we can obtain following ordinary differential equations:

$$\frac{\partial}{\partial z}\frac{f_0^2}{N^2}\frac{\partial}{\partial z}\hat{\Psi}^{sur}-\kappa^2\hat{\Psi}^{sur}=0 \tag{A3a}$$

$$\left.\frac{d\hat{\Psi}^{sur}}{dz}\right|_{z=0}=\frac{\hat{b}^s(k,l)}{f_0} \tag{A3b}$$

$$\left.\frac{d\hat{\Psi}^{sur}}{dz}\right|_{z=-H}=0, \tag{A3c}$$

and

$$\frac{\partial}{\partial z}\frac{f_0^2}{N^2}\frac{\partial}{\partial z}\hat{\Psi}^{\text{int}}-\kappa^2\hat{\Psi}^{\text{int}}=\hat{q} \tag{A4a}$$

$$\left.\frac{d\hat{\Psi}^{\text{int}}}{dz}\right|_{z=0,\,-H}=0, \tag{A4b}$$

where $\kappa=(k^2+l^2)^{1/2}$ is the magnitude of the horizontal wavenumber, and the hat stands for the horizontal Fourier transform. For given sea surface buoyancy field and stratification, equation (A3a) can be solved directly.

On the other hand, the interior solution $\hat{\Psi}^{\text{int}}$ cannot be directly determined from equation (A4a) because the interior PV anomaly $\hat{q}$ is unknown. However, with the knowledge of surface pressure (height), the interior solution can be derived through a different approach, given the projection of $\hat{\Psi}^{\text{int}}$ onto vertical normal modes:

$$\hat{\Psi}^{\text{int}}(k,l,z)=\sum_n A_n(k,l)F_n(z). \tag{A5}$$

The vertical normal modes $F_m(z)$ are solutions to the Sturm-Liouville problem [*Pedlosky*, 1987]:

$$\frac{\partial}{\partial z}\left(\frac{f_0^2}{N^2}\frac{\partial F_m}{\partial z}\right)=-R_m^{-2}F_m, \tag{A6}$$

with the same boundary conditions as for Ψ^{int}. Here R_m is the mth Rossby deformation radius. $F_m(z)$ can be solved numerically given stratification $N^2(z)$.

Truncating the interior solution to the two gravest (barotropic and first baroclinic) modes [*Wang et al.*, 2013], expression (A5) can be approximated as:

$$\hat{\Psi}^{\text{int}}(k,l,z)=A_0(k,l)F_0(z)+A_1(k,l)F_1(z). \tag{A7}$$

Both SQG and interior solutions contribute to the sea surface height (pressure) anomaly and bottom pressure anomaly:

$$\hat{\Psi}^{sur}(k,l,0)+\hat{\Psi}^{\text{int}}(k,l,0)=\frac{g}{f_0}\hat{\eta}(k,l), \tag{A8a}$$

$$\hat{\Psi}^{sur}(k,l,-H)+\hat{\Psi}^{\text{int}}(k,l,-H)=0, \tag{A8b}$$

where η is SSH anomaly. Substituting (A7) into equation (A8), with the surface height observation, $\hat{\Psi}^{sur}$ calculated from equation (A3a), and $F_m(z)$ obtained from equation (A6), we can determine the two modal coefficients A_0 and A_1 via Cramer's rule. Thus, interior solution $\hat{\Psi}^{\text{int}}$ and the total solution Ψ can be obtained.

Furthermore, eddy density and velocity are deduced from the retrieved geostrophic stream function according to $\rho^a=-\frac{\rho_0 f}{g}\frac{\partial\Psi}{\partial z}$ and $\vec{V}=\hat{z}\times\nabla\Psi$.

Acknowledgments

This work was jointly supported by the MOST of China (grant 2014CB953904), the Strategic Priority Research Program of the Chinese Academy of Sciences (grant XDA11010304), National Natural Science Foundation of China (grants 41521005, 41376021, and 41676016). We are grateful to the freely available data for this paper: SSH distributed by AVISO (http://www.aviso.altimetry.fr); SST field from AVHRR (https://www.ncdc.noaa.gov/oisst); SMOS SSS (http://www.catds.fr); YoMaHa'07 (http://www.apdrc.soest.hawaii.edu); AGVA (http://www.flux.ocean.washington.edu); and ISAS-13 T/S fields (http://www.argo.ucsd.edu/). The Argo data were collected and made freely available by the International Argo Program and the national programs that contribute to it (http://www.argo.ucsd.edu, http://www.jcommops.org/argo). The Argo Program is part of the Global Ocean Observing System. Thanks also go to Dr. Jinbo Wang for helpful comments and the anonymous reviewers for their valuable suggestions.

References

Blumen, W. (1978), Uniform potential vorticity flow. Part I: Theory of wave interactions and two-dimensional turbulence, *J. Atmos. Sci.*, *35*, 774–783.

Boutin, J., N. Martin, G. Reverdin, X. Yin, and F. Gaillard (2013), Sea surface freshening inferred from SMOS and Argo salinity: Impact of rain, *Ocean Sci.*, *9*, 183–192, doi:10.5194/os-9-183-2013.

Bretherton, F. P. (1966), Critical layer instability in baroclinic flows, *Q. J. R. Meteorol. Soc.*, *92*, 325–334.

Carnes, M. R., J. L. Mitchell, and P. W. deWitt (1990), Synthetic temperature profiles derived from Geosat altimetry: Comparison with air-dropped expendable bathythermograph profiles, *J. Geophys. Res.*, *95*, 17,979–17,992.

Carnes, M. R., W. J. Teague, and J. L. Mitchell (1994), Inference of subsurface thermohaline structure from fields measurable by satellite, *J. Atmos. Oceanic Technol.*, *11*, 551–566.

Charney, J. G. (1971), Geostrophic turbulence, *J. Atmos. Sci.*, *28*, 1087–1095.
Chavanne, C. P., and P. Klein (2010), Can oceanic submesoscale processes be observed with satellite altimetry? *Geophys. Res. Lett.*, *37*, L22602, doi:10.1029/2010GL045057.
Chelton, D., and M. Schlax (2003), The accuracies of smoothed sea surface height fields constructed from tandem altimeter datasets, *J. Atmos. Oceanic Technol.*, *20*, 1276–1302.
Cooper, M., and K. Haines (1996), Altimetric assimilation with water property conservation, *J. Geophys. Res.*, *101*, 1059–1077, doi:10.1029/95JC02902.
Dibarboure, G., M.-I. Pujol, F. Briol, P.-Y. Le Traon, G. Larnicol, N. Picot, F. Mertz, and M. Ablain (2011), Jason-2 in DUACS: Updated system description, first tandem results and impact on processing and products, *Mar. Geod.*, *34*, 214–241.
Ducet, N., P.-Y. Le Traon, and G. Reverdin (2000), Global high-resolution mapping of ocean circulation from TOPEX/Poseidon and ERS-1 and-2, *J. Geophys. Res.*, *105*, 19,477–19,498.
Ferrari, R., and C. Wunsch (2010), The distribution of eddy kinetic and potential energies in the global ocean, *Tellus Ser. A*, *62*, 92–108.
Fu, L.-L., and C. Ubelmann (2014), On the transition from profile altimeter to swath altimeter for observing global ocean surface topography, *J. Atmos. Oceanic Technol.*, *31*, 560–568.
Gaillard, F. (2012), ISAS-tool version 6: Method and configuration, *report LPO-12-02*, 18 pp., Laboratoire de Physique des Océans (LPO).
Gaillard, F., E. Autret, V. Thierry, P. Galaup, C. Coatanoan, and T. Loubrieu (2009), Quality control of large Argo datasets, *J. Atmos. Oceanic Technol.*, *26*, 337–351.
Gaultier, L., C. Ubelmann, and L.-L. Fu (2016), The challenge of using future SWOT data for oceanic field reconstruction, *J. Atmos. Oceanic Technol.*, *33*, 119–126.
González-Haro, C., and J. Isern-Fontanet (2014), Global ocean current reconstruction from altimetric and microwave SST measurements, *J. Geophys. Res. Oceans*, *119*, 3378–3391, doi:10.1002/2013JC009728.
Gray, A. R., and S. C. Riser (2014), A global analysis of Sverdrup balance using absolute geostrophic velocities from Argo, *J. Phys. Oceanogr.*, *44*, 1213–1229.
Haines, K. (1991), A direct method for assimilating sea surface height data into ocean models with adjustments to the deep circulation, *J. Phys. Oceanogr.*, *21*, 843–868.
Hakim, G. J., C. Snyder, and D. J. Muraki (2002), A new surface model for cyclone-anticyclone asymmetry, *J. Atmos. Sci.*, *59*, 2405–2420.
Held, I. M., R. T. Pierrehumbert, S. T. Garner, and K. L. Swanson (1995), Surface quasigeostrophic dynamics, *J. Fluid Mech.*, *282*, 1–20.
Hoskins, B. J. (1975), The geostrophic momentum approximation and the semi-geostrophic equations, *J. Atmos. Sci.*, *32*, 233–242.
Hurlburt, H. E. (1986), Dynamic transfer of simulated altimeter data into subsurface information by a numerical ocean model, *J. Geophys. Res.*, *91*, 2372–2400.
Isern-Fontanet, J., B. Chapron, G. Lapeyre, and P. Klein (2006), Potential use of microwave sea surface temperatures for the estimation of ocean currents, *Geophys. Res. Lett.*, *33*, L24608, doi:10.1029/2006GL027801.
Isern-Fontanet, J., G. Lapeyre, P. Klein, B. Chapron, and M. W. Hecht (2008), Three dimensional reconstruction of oceanic mesoscale currents from surface information, *J. Geophys. Res.*, *113*, C09005, doi:10.1029/2007JC004692.
Isern-Fontanet, J., M. Shinde, and C. González-Haro (2014), On the transfer function between surface fields and the geostrophic stream function in the Mediterranean Sea, *J. Phys. Oceanogr.*, *44*, 1406–1423, doi:10.1175/JPO-D-13-0186.1.
Juckes, M. (1994), Quasigeostrophic dynamics of the tropopause, *J. Atmos. Sci.*, *51*, 2756–2768.
Klein, P., B. L. Hua, G. Lapeyre, X. Capet, S. L. Gentil, and H. Sasaki (2008), Upper ocean turbulence from high-resolution 3D simulations, *J. Phys. Oceanogr.*, *38*, 1748–1763.
Klein, P., J. Isern-Fontanet, G. Lapeyre, G. Roullet, E. Danioux, B. Chapron, S. Le Gentil, and H. Sasaki (2009), Diagnosis of vertical velocities in the upper ocean from high resolution sea surface height, *Geophys. Res. Lett.*, *36*, L12603, doi:10.1029/2009GL038359.
LaCasce, J. H. (2012), Surface quasigeostrophic solutions and baroclinic modes with exponential stratification, *J. Phys. Oceanogr.*, *42*, 569–580.
LaCasce, J. H., and A. Mahadevan (2006), Estimating subsurface horizontal and vertical velocities from sea surface temperature, *J. Mar. Res.*, *64*, 695–721.
LaCasce, J. H., and J. Wang (2015), Estimating subsurface velocities from surface fields with idealized stratification, *J. Phys. Oceanogr.*, *45*, 2424–2435.
Lapeyre, G., and P. Klein (2006), Dynamics of the upper oceanic layers in terms of surface quasigeostrophy theory, *J. Phys. Oceanogr.*, *36*, 165–176.
Lebedev, K. V., H. Yoshinari, N. Maximenko, and P. W. Hacker (2007), YoMaHa'07: Velocity data assessed from trajectories of Argo floats at parking level and at the sea surface, *Tech. Note 4(2)*, 16 pp., Int. Pac. Res. Cent., Univ. of Hawaii, Honolulu.
Le Traon, P. Y., P. Klein, B. L. Hua, and G. Dibarboure (2008), Do altimeter wavenumber spectra agree with the interior or surface quasigeostrophic theory?, *J. Phys. Oceanogr.*, *38*, 1137–1142.
Liu, L., S. Peng, J. Wang, and R. X. Huang (2014), Retrieving density and velocity fields of the ocean's interior from surface data, *J. Geophys. Res. Oceans*, *119*, 8512–8529, doi:10.1002/2014JC010221.
McClean, J. L., P.-M. Poulain, J. W. Pelton, and M. E. Maltrud (2002), Eulerian and Lagrangian statistics from surface drifters and a high-resolution POP simulation in the North Atlantic, *J. Phys. Oceanogr.*, *32*, 2472–2491.
Pedlosky, J. (1987), *Geophysical Fluid Dynamics*, 2nd ed., 728 pp., Springer-Verlag, New York.
Ponte, A. L., and P. Klein (2013), Reconstruction of the upper ocean 3D dynamics from high resolution sea surface height, *Ocean Dyn.*, *63*(7), 777–791.
Qiu, B., S. Chen, P. Klein, C. Ubelmann, L.-L. Fu, and H. Sasaki (2016), Reconstructability of three-dimensional upper-ocean circulation from SWOT sea surface height measurements, *J. Phys. Oceanogr.*, *46*, 947–963.
Reul, N., and Ifremer CATDS-CECOS Team (2011), *SMOS L3 SSS Research Products: Product User Manual Reprocessed Year 2010*, IFREMER, Plouzané, France.
Reul, N., B. Chapron, T. Lee, C. Donlon, J. Boutin, and G. Alory (2014), Sea surface salinity structure of the meandering Gulf Stream revealed by SMOS sensor, *Geophys. Res. Lett.*, *41*, 3141–3148, doi:10.1002/2014GL059215.
Reynolds, R. W. (2009), What's new in version 2. OISST, webpage, NOAA/NCEI. [Available at www.ncdc.noaa.gov/sites/default/files/attachments/Reynolds2009_oisst_daily_v02r00_version2-features.pdf.]
Reynolds, R. W., T. M. Smith, C. Liu, D. B. Chelton, K. S. Casey, and M. G. Schlax (2007), Daily high-resolution-blended analyses for sea surface temperature, *J. Clim.*, *20*, 5473–5496.
Rio, M., S. Guinehut, and G. Larnicol (2011), New CNES-CLS09 global mean dynamic topography computed from the combination of GRACE data, altimetry, and in situ measurements, *J. Geophys. Res.*, *116*, C07018, doi:10.1029/2010JC006505.

Smith, R. D., M. E. Maltrud, F. O. Bryan, and M. W. Hecht (2000), Numerical simulation of the North Atlantic ocean at 1/10 degree, *J. Phys. Oceanogr.*, *30*(7), 1532–1561.

Tulloch, R., and K. S. Smith (2006), A theory for the atmospheric energy spectrum: Depth-limited temperature anomalies at the tropopause, *Proc. Natl. Acad. Sci. U. S. A.*, *51*, 2756–2768.

Tulloch, R., and K. S. Smith (2009), Quasigeostrophic turbulence with explicit surface dynamics: Application to the atmospheric energy spectrum, *J. Atmos. Sci.*, *66*, 450–467.

Wang, J., G. Flierl, J. LaCasce, J. McClean, and A. Mahadevan (2013), Reconstructing the ocean's interior from surface data, *J. Phys. Oceanogr.*, *43*, 1611–1626, doi:10.1175/JPO-D-12-0204.1.

Watts, D. R., C. Sun, and S. Rintoul (2001), A two-dimensional gravest empirical mode determined from hydrographic observations in the Subantarctic front, *J. Phys. Oceanogr.*, *31*, 554–571.